Article

Spatio-Temporal Variability of Suspended Particulate Matter in a High-Arctic Estuary (Adventfjorden, Svalbard) Using Sentinel-2 Time-Series

Daniela M. R. Walch [1,2,3,*], Rakesh K. Singh [3], Janne E. Søreide [1], Hugues Lantuit [2,4] and Amanda Poste [5,6]

1 Arctic Biology Department, The University Centre in Svalbard (UNIS), P.O. Box 156, 9171 Longyearbyen, Norway; janne.soreide@unis.no
2 Insititut für Umweltwissenschaften und Geografie, Universität Potsdam, 14461 Potsdam, Germany; hugues.lantuit@awi.de
3 Département de Biologie, Chimie et Géographie, Université du Québec à Rimouski, Rimouski, QC G5L 3A1, Canada; rakeshkstp@gmail.com
4 Permafrost Research Section, Alfred Wegener Institute for Polar and Marine Research, 14473 Potsdam, Germany
5 Norwegian Institute for Water Research (NIVA), Fram Centre for High North Research, Hjalmar Johansens Gate 14, 9007 Tromsø, Norway; amanda.poste@niva.no
6 Department of Arctic and Marine Biology, UiT: The Arctic University of Norway, P.O. Box 6050, 9037 Tromsø, Norway
* Correspondence: wald0001@uqar.ca

Abstract: Arctic coasts, which feature land-ocean transport of freshwater, sediments, and other terrestrial material, are impacted by climate change, including increased temperatures, melting glaciers, changes in precipitation and runoff. These trends are assumed to affect productivity in fjordic estuaries. However, the spatial extent and temporal variation of the freshwater-driven darkening of fjords remain unresolved. The present study illustrates the spatio-temporal variability of suspended particulate matter (SPM) in the Adventfjorden estuary, Svalbard, using in-situ field campaigns and ocean colour remote sensing (OCRS) via high-resolution Sentinel-2 imagery. To compute SPM concentration ($C_{\text{SPM}_{\text{sat}}}$), a semi-analytical algorithm was regionally calibrated using local in-situ data, which improved the accuracy of satellite-derived SPM concentration by ~20% (MRD). Analysis of SPM concentration for two consecutive years (2019, 2020) revealed strong seasonality of SPM in Adventfjorden. Highest estimated SPM concentrations and river plume extent (% of fjord with $C_{\text{SPM}_{\text{sat}}} > 30$ mg L^{-1}) occurred during June, July, and August. Concurrently, we observed a strong relationship between river plume extent and average air temperature over the 24 h prior to the observation ($R^2 = 0.69$). Considering predicted changes to environmental conditions in the Arctic region, this study highlights the importance of the rapidly changing environmental parameters and the significance of remote sensing in analysing fluxes in light attenuating particles, especially in the coastal Arctic Ocean.

Keywords: ocean colour; coastal darkening; SPM; sediment plumes; Arctic coast; remote sensing; regional tuning; coastal ecosystems; land-ocean-interaction; riverine inputs

1. Introduction

Changes to the Arctic have been well-documented, including increasing annual temperature and precipitation as well as distinct changes in seasonality [1–3]. These changes can be expected to affect catchment processes in Arctic river systems and impact adjacent coastal ecosystems through an increase in melting and drainage of glaciers during the ablation season [4], permafrost thaw [5,6] and more general shifts in the local water budget by extreme weather events such as heavy rainfall events [1].

Estuaries and fjords, as a specific type of coast, are characterised by strong physico-chemical gradients from land to sea [7]. These gradients vary corresponding to the distance from land and river outlets as well as coastal geomorphology. Riverine inputs, especially to these fjord-type estuaries [8,9], demonstrate strong variability in levels of particle load and distribution over a hydrological year [10] and have the potential to support primary production through delivery of terrestrial nutrients [11,12]. Environmental conditions in these transition zones are, thus, driven by tides, wind, as well as fluxes of freshwater, nutrients, and organic matter [12–15].

Water quality is a crucial assessment in these "Aquatic Critical Zones" [16], commonly through the characterisation of concentrations of chlorophyll-a (Chl-a), chromophoric dissolved organic matter (CDOM), turbidity and suspended particulate matter (SPM). The latter is the key driver of light attenuation in surface waters [17] as it increases scattering of incoming light [18]. Thus, high turbidity in sediment-laden freshwater plumes and comparably high amounts of CDOM may limit light availability for coastal phytoplankton and benthic primary producers [12,19,20]. Coastal darkening [21,22] refers to this ongoing change through increased light attenuation from terrestrial inputs in coastal ecosystems, which results in decreased benthic light availability. SPM may consist of organic and inorganic material [23]. In highly sedimentary environments, such as fjordic estuaries that are characterised by glaciogenic sediment delivery during the ablation season [24], SPM can be used as a proxy for estimation of sediment fluxes in these transition zones [25–27].

Polar warming, driving increased glacial river runoff [28], as well as an increase in precipitation [1] and coastal erosion may lead to massive sediment plumes along Arctic coastlines [29] such as in the archipelago of Svalbard. These plumes vary rapidly on spatio-temporal scales and hence, estimating the extent by traditional in-situ measurements is challenging. Consequently, ocean colour remote sensing (OCRS) for water quality monitoring has become more and more important [30] and analysis of satellite imagery for water quality monitoring at lower spatial resolution for off-shore applications and in lower latitudes is now quite common. The use of optical satellite imagery at high to medium resolution has, however, only seldomly been applied to the narrow and optically complex environments of polar fjords and estuaries [31,32], but is likely to improve our understanding of dynamic changes that occur over seasonal and shorter time scales (e.g., in response to extreme weather events or tidal cycles) and/or over a range of spatial scales (very local effects and regional patterns). Additionally, in polar regions, and even more so along the vast coasts that host areas of enhanced productivity, sufficient ground-truthing datasets for the validation of arctic tuned OCRS algorithms and consistent analysis remain scarce. With growing applications of remote observations in the polar regions from multispectral imagery [31,33–36], datasets of matchup are of increasing importance.

One of the greatest challenges associated with OCRS at higher latitudes is the dependency on favourable weather conditions: fjords and other nearshore environments are prone to higher levels of air moisture, often resulting in haze and clouds [37]. This is especially true during the high Arctic summer [38,39]. Polar-orbiting satellite missions overcome these limitations by featuring a higher temporal resolution with multiple overpasses per day during the summer season. In particular, the Sentinel-2 mission (ESA Copernicus), with its twin-satellites (S2A and S2B) equipped with MultiSpectral Imager (MSI) sensors, is providing high resolution and high frequency monitoring of Arctic regions, allowing for more cloud-free images over the course of a season. They operate with a primary focus on land imaging since 2015 and 2017 for S2A and S2B, respectively, and record 13 bands between violet and near-infrared at high to medium spatial resolution (band dependent between 10–60 m).

OCRS algorithms for turbidity [40] and SPM [41] in coastal areas have become a new asset. A wide range of ratio-based [26] and semi-analytical approaches for retrieving water quality parameters such as SPM from optical satellite imagery exists. An in-depth discussion of the performances can be found elsewhere (e.g., [42,43]) and would go beyond the scope of this introduction. Briefly, band-ratio algorithms rely on direct empirical

relationships between in-situ concentrations of SPM (C_{SPM}) and recorded reflectance [26,44] and are, as such, data-driven [43] They can be distinguished from analytical or semi-analytical algorithms [41] that build (at least in part) on physical assumptions of the interaction between light and the parameter in question [43].

Studies emphasise the use of switching or algorithms to avoid saturation of the algorithm at use of a single-band [42]. Classically, reflectance in the red (for instance at 665 nm in the case of MSI) would in this case be used up to a threshold value of C_{SPM}, while for very high C_{SPM} longer wavelengths in the near infrared (at 865 nm), seem to model these concentrations more accurately. For highly productive fjordic areas, we have, however, to consider the possibility of misclassification of elevated signals in the near infrared—due to increased chlorophyll concentrations—as SPM [45]. Therefore, for this study, a single-band approach was chosen based on solely the red channel (at 665 nm). Therefore, a single-band approach based on the red channel was chosen to model C_{SPM} in the present study.

AOPs depend upon many region-specific chemical and physical factors (given by the IOPs) as well as the light field, and algorithms developed for the open ocean or other coastal regions may not be applicable to Arctic coasts. Klein et al. [35] therefore recently used in-situ measurements to regionally calibrate a turbidity model [40] for the Arctic nearshore zone of Herschel Island, Canada. Regional tuning of the existing generic algorithms for SPM [41,46,47] offers the possibility to build a strong RS-based dataset with high temporal and spatial resolution. Although the matchup cal/val dataset established for this study encompasses multiple days of measurements, it is not suitable for empirical single-band or band-ratio approaches [46] as they gain accuracy with the number of observations used as input. We therefore used the calibration dataset and statistical tools to regionally calibrate the semi-analytical single-band SPM algorithm, first introduced by Nechad et al. [41] (here named NeCal). We call this calibrated model 'AdvFCal' for this specific study, which enabled the observation of the seasonal evolution of modelled C_{SPM} and plume extent in Adventfjorden as well as the statistical evaluation of a set of potential environmental drivers.

With our study, the general goal was to enhance our understanding of the physicochemical conditions in highly dynamic coastal ecosystems, specifically the estuary of Adventfjorden, by following the objectives to (1) calibrate and validate (cal/val) the OCRS SPM algorithm and assess its performance, (2) analyse the spatial and temporal variability of C_{SPM} based on in-situ and Sentinel-2 data, and finally (3) couple time-series data of RS-derived SPM ($C_{SPM_{sat}}$) with additional meteorological and hydrological datasets to explore existing relationships with environmental drivers.

2. Materials and Methods

2.1. Study Site

Adventfjorden is one of several inner fjord arms in Isfjorden, a fjord system on the west coast of Spitsbergen in the archipelago of Svalbard, Norway [48]. The fjord is 8.3 km long and 3.4 km wide and has a northwest orientation within 78°13' and 78°17'N and 15°25' and 15°46'E [49] (Figure 1). A recent report highlighted the climate changes to this region, such as the ongoing rise in average annual temperature and the seasonality in precipitation [1]. The largest settlement of Svalbard, Longyearbyen, lies at the southwest shore of the fjord. Situated near the University Centre in Svalbard (UNIS), Adventfjorden offers high accessibility and short transport and processing time for field samples.
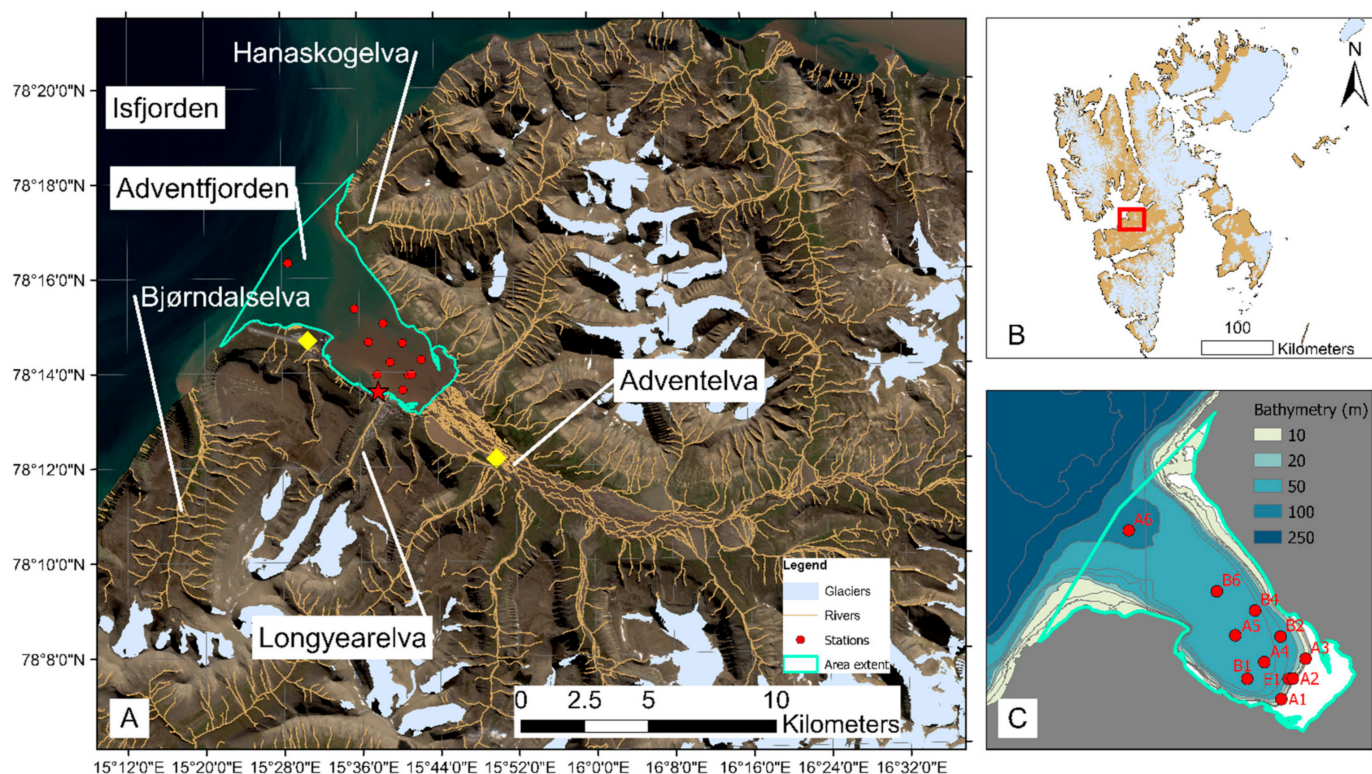
Figure 1. (**A**) Map of the Adventfjorden study area and the catchment of Adventelva and Longyearelva. Longyearbyen is marked with a red star. Yellow squares mark monitoring stations for weather (at Longyearbyen Airport) and river-hydrology (monitoring station operated by NIVA at Aventelva), (**B**) Overview of the study region in Svalbard archipelago, the highlighted outline indicating the area of interest (AOI) shown in (**A,C**) Station map of Adventfjorden for 2019 and 2020 field campaigns within the area extent defined for Adventfjorden for the purpose of this study.(map was created based on S-100 vector data provided by Norwegian Polar Institute [50]; bathymetry data from the Norwegian Mapping Authority [51]; contains modified Copernicus Sentinel-2 data (2020, Sentinel-2 B image 27 July 2020) processed by Sentinel-Hub (https://scihub.copernicus.eu/, accessed: 28 June 2021).

Adventdalen is a broad U-shaped valley with a catchment area of more than 500 km^2 [2,52]. The main discharging river is the strongly braided river Adventelva. A recent report indicate an increase in mean annual freshwater fluxes in the Adventelva river over the last two decades, with discharge reaching as high as 376,143 $\times 10^3$ m^3 per year (averaged over the years 2011–2019) [2]. The fjord is fed by several land-terminating glaciers [52,53] and receives discharge from the rivers Adventelva and Longyearelva, as well as several smaller river systems [48]. Thus, glaciogenic particles being mobilised throughout the ablation season dominate the suspended sediments in the runoff to the fjord [52,54].

Generally, fjords are areas of sediment deposition, especially in close proximity to river outlets [8,24], while transport to the outer parts of the fjord is limited by grain size of the transported sediments [49]. Riverine transport of terrigenous material to Adventfjorden is limited to approximately four months of the year, when the rivers and tributaries are flowing [55]. The fjord features seasonal ice-cover [55,56], but has remained without a solid sea-ice cover for several years [57], thus it is commonly regarded as ice-free. It should be noted that the studied year 2020 was an exception, when extensive ice-cover was observed in the fjord.

2.2. In-Situ Measurements

Field sampling and collection of in-situ data was carried out on 10 occasions in 2019 and 2020. Field work was carried out on small open boats and consisted of the collection of surface water samples from a station grid in Adventfjorden (n = 11 stations) that was designed to cover the main plume area. To capture the variability of values for SPM in the fjord, a transect from inner to outer fjord (stations A2, A4, A5, B6, A6, see Figure 1) was prioritised in the sampling campaigns, as was one cross-section close to the tidal flat (A1–A3) when sampling time was limited. Sampling days were planned to coincide with Sentinel-2 (S2A and S2B) overpasses and (where possible) clear skies, allowing for the in-situ samples to be used as a ground truth dataset to match-up with corresponding cloudless satellite images. The duration of field campaigns varied between two to five hours depending on the number of measurements and water samples taken. This resulted in varying differences between the in-situ sampling and the satellite passing, which occurred between 12:00 and 13:30 (UTC) on average.

Water samples were collected from the uppermost 10–20 cm of surface water with a clean stainless-steel bucket, pre-screened through 200 μm mesh to remove larger zooplankton and transferred into a well-rinsed opaque 5 L carboy. Samples were kept cool in a dark transport cooler box until further processing at the University Centre in Svalbard (UNIS). Secchi depth Z_{SD} was recorded on every station using a standardised secchi disk and a measuring tape lowered from the shadow side of the vessel. A handheld turbidity meter (TN-100 model, Thermo Scientific Eutech) was used to record T in NTU (Nephelometric Turbidity Unit) from well-mixed samples immediately after collection. In this study, measurements of turbidity were taken as triplicates at each station in 2019 only since the instrument was not available for use during the field operations in 2020. Averaged values of turbidity per station were used for further analysis.

C_{SPM} in the surface water of Adventfjorden was determined for n = 96 surface samples, over the course of the two ablation seasons in 2019 and 2020, respectively (see Supplementary Table S1). SPM concentration is calculated from laboratory filtration of water samples through filters with commonly 0.7 μm pore size [58] via gravimetric methods (e.g., [23]). To determine the dry weight of SPM (hereon SPM$_{insitu}$), the obtained water samples were filtered through pre-combusted, pre-weighed 47 mm GF/F glass microfibre filters (Whatman$^{®}$) with a nominal pore size of 0.7 μm [23], following protocols of previous work in the FreshFate project (see [12]). Filtration of samples took place promptly, with the time between field sampling and processing rarely exceeding four hours. Maximum filtration volumes were chosen according to total available sample volume and the present water clarity at the station. The final filtration volume was noted, the filters were transferred into petri dishes (FALCON$^{®}$, 50 mm × 9 mm) and stored horizontally in the dark at −20 °C until further analysis (within two months of collection). Filters were dried at 104 °C for 60 min, then cooled in a desiccator. This drying process was repeated until the weight was stable (mass loss of less than 4% or 0.04 mg between weighing). The final concentration of $C_{SPM_{insitu}}$ (mg L^{-1}) was determined from the difference in weight of the filter before and after filtration (in mg) divided by the filtration volume (in L).

2.3. Sentinel-2 Satellite Imagery

In aquatic applications of Earth Observation (EO), airborne and satellite-based remote sensing (RS) are used to assess the magnitude and variability of optically active constituents (OACs), such as SPM, present in the water body. The Inherent Optical Properties (IOPs) of these result in different spectral patterns due to selective absorption (a) and scattering (b) in the backward direction (b_b) [59]. Ocean Colour Remote Sensing (OCRS) is, thus, used to estimate the concentration of the OACSs with a high-degree of accuracy [60,61] by building on inverse relationships between IOP, which are independent on the geometry of the incident and reflected light, and apparent optical properties (AOP, i.e., the water's

colour) recorded as remote sensing reflectance R_{rs}. The water-leaving reflectance ρ_w, which is more commonly used in OCRS, is calculated from R_{rs},

$$\rho_w(\lambda) = \pi \times R_{rs}(\lambda) \tag{1}$$

For this study, available Copernicus Sentinel 2019 and 2020 data, that is S2A and S2B Level 1C (L1C) images were downloaded from the Copernicus Open Access Hub (European Space Agency, ESA) consisting of calibrated top-of-the-atmosphere (TOA) reflectance values. Images throughout the sensing period 01 March 2019 to 30 September 2019 and 01 March 2020 to 30 September 2020 that fit the criteria were further investigated as potential data based on the relative cloud cover present in the image at the time of the observation. The threshold for the selection was set to 50% cloud cover to account for the potential valid observations over the area of interest (AOI), Adventfjorden.

The TOA reflectance from the L1C images was corrected for the influence of atmospheric scattering, which includes scattering by air molecules and aerosols, along with the surface scattering in the form of, for instance, sun-glint [62,63]. This correction of TOA reflectance to calculate bottom of atmosphere (BOA) reflectance, called atmospheric correction (AC), is a crucial part of OCRS. Over optically complex coastal and inland water surfaces, AC is a challenging process and may lead to large differences between satellite estimates and in-situ conditions [62]. The remote sensing reflectance (R_{rs}) was, therefore, determined from the L1C products by the ocean colour processing software SeaDAS v7.5.3 (SeaWiFS Data Analysis System, NASA) with a modified aerosol correction method adapted for optically complex and turbid water masses, called SSP aerosol correction algorithm [62], which computed aerosol radiance in the coastal waters of a highly sedimentary estuary with exceptional accuracy. Therefore, SSP is used in the present study. Due to lacking validation reflectance data, we were not able to perform the validation of the here-chosen AC for Adventfjorden. The application of this AC workflow has been, however, recently evaluated for very turbid waters of the St. Lawrence estuary and James Bay, Canada [64] and showed good results for the red band of the MSI sensor onboard Sentinel-2. Using this adapted AC within the framework of the SeaDAS command line allowed for the automated processing of all available images.

An initial number of 181 images had to be reduced to 116 based on requirements for cloud presence over the area of interest. The images were cropped to the area of interest. The land and clouds were masked, leaving the area of Adventfjorden, from the tidal flat to the farthest station A6 for time-series and statistical analysis.

2.4. Calibration and Validation of the SPM Algorithm

The semi-analytical single-band SPM algorithm introduced by [41] assumes that the IOPs of suspended particles are directly proportional to C_{SPM}, with negligible influence from other (non-particulate) constituents. By applying these assumptions, C_{SPM} may be calculated as [41]

$$C_{SPM} = \frac{A^\rho \rho_w(665)}{1 - \rho_w(665)/C^\rho} + B^\rho \tag{2}$$

where ρ_w is the water-leaving reflectance, and A^ρ $(g\, m^{-3})$ and C^ρ are coefficients representing IOPs of the water column (i.e., algal and non-algal particles). B^ρ is an offset to avoid underestimation by the model at low SPM concentrations [41,42]. This generic algorithm was originally calibrated based on data from the southern North Sea [41] and should therefore be re-calibrated to suit the regional characteristics of waters in Arctic Adventfjorden, which is impacted by high sediment loads from land-terminating glaciers in the adjacent catchment.

Given the characteristic signature of absorption, the choice of wavelength (and the corresponding band in the sensor) can influence the accuracy of $\rho_w(\lambda)$ estimates significantly [42,46,65]. This study used ρ_w at the red band of the Sentinel-2 MSI sensors (λ = 665 nm) to derive remotely sensed values SPM (here on, C_{SPMsat}). The red band was

chosen as Chl-a exhibits an absorption maximum in the red band while the reflectance of sediments is significantly high, which will reduce potential misclassification of phytoplankton particles as SPM for the purpose of this study.

Non-linear least squared analysis was then performed on a calibration dataset for $C_{SPM_{insitu}}$ against the pixel value for the reflectance $\rho_w(665)$ in Python v3.7.9 using the open-source SciPy package [66] and averaging 100 rounds of random subsamples. Bounds for the three coefficients (A, B and C in Equation (2)) were chosen in accordance with the suggestions in Nechad et al. [41] for the chosen band wavelength of 665 nm. The calculated $C_{SPM_{sat}}$ data was then tested against $C_{SPM_{insitu}}$ measurements from the field campaign. The performance of the calibration was assessed with the standard measurement of the normalised root-mean-square difference (RMSD), the mean relative difference (MRD), and bias, which are used in performance testing of modelled values in OCRS [62,67]. These were calculated as

$$MRD = \frac{1}{n} \sum \frac{C_{SPM_{sat}} - C_{SPM_{insitu}}}{C_{SPM_{insitu}}} \times 100 \tag{3}$$

$$RMSD = \sqrt{\frac{1}{n} \sum \left(C_{SPM_{insitu}} - C_{SPM_{sat}}\right)^2} \tag{4}$$

$$Bias = \frac{1}{n} \sum \left(C_{SPM_{insitu}} - C_{SPM_{sat}}\right) \tag{5}$$

where n is the number of observations.

2.5. Environmental Datasets

Weather data, recorded at the nearest permanently operated weather station (Svalbard airport [68]) was downloaded from the Norwegian MET service homepage [69]. The values were processed and used as background data for regression analysis, i.e., environmental forcing of freshwater-derived turbid river plumes in Adventfjorden. Daily averages of air temperature (°C) and wind speed (ms^{-1}) as well as sums of precipitation are used to describe the meteorology present in Adventfjorden over the course of the studied period. Tidal data for the semi-diurnal tidal regime of Adventfjorden (~104 cm tidal range) was downloaded for Longyearbyen and Adventfjorden as recorded by Norwegian Mapping Authorities, Hydrographic Service [70]. The tide tables are openly accessible. In-situ sensor-based monitoring platforms are operated by the Norwegian Institute for Water Research (NIVA, PI: Amanda Poste) in the Adventelva river. The river mooring is typically deployed in mid-June and retrieved in late September, and provides continuous measurements of temperature, conductivity, and pH (2017–2020); turbidity (2019–2020); and water level (2017–2019). Here, values for turbidity and water level were used.

2.6. Time-Series Analysis and Environmental Statistics

A workflow in R 4.1.0 [71], was used for further processing based on the packages "raster" [72] and "ncdf4" [73]. The regionally adapted coefficients for the OCRS Nechad et al. [41] SPM algorithm were applied using $\rho_w(665)$ values from L2 processed images to retrieve $C_{SPM_{sat}}$, with a maximum 500 mg L^{-1} $C_{SPM_{sat}}$ defined as valid observations per pixel. Projected image stacks for 2019–2020 of satellite images were created. Additional bands were calculated, including statistical information per temporally binned pixel. More specifically minimum (min), maximum (max), standard deviation (SD), coefficient of variation (CV), mean, median, and finally the number of valid observations. The images with zero valid observations were discarded. Pixel values of $C_{SPM_{sat}}$ were extracted from all images. Based on this dataset, elementary statistics were applied to all images (i.e., minimum, maximum, mean, median, interquartile range (IQR)) based on the total number of available pixels per image.

For the analysis of the spatial extent of very turbid sediment-laden freshwater plumes in Adventfjorden, that we call the river plume, a threshold value for $C_{SPM_{sat}}$ of 30 mg L^{-1} was identified from processed images and modelled $C_{SPM_{sat}}$ and is furthermore based on

Secchi depth (Z_{SD}) being less than 1 m for most occasions where $C_{SPM_{insitu}}$ observations reached or exceeded 30 mg L^{-1}. In a comparable study on OCRS of sediment plumes, [74] defined 10 mg L^{-1} as a threshold. However, in the highly sedimentary systems of Svalbard this value might be easily exceeded, hence, a higher value was chosen to differentiate between distinct river plumes and assess its seasonal variability. This threshold value functions as a mask to the time-series data, and the relative area of the fjord covered with the river plume was estimated with the following equation.

$$\text{Pixel}_{\text{plume}}[\%] = \frac{N_{>30}}{N} \times 100 \tag{6}$$

Here, $N_{>30}$ depicts the number of pixels with $C_{SPM_{sat}}$ greater than 30 mg L^{-1} and N is the total number of pixels in the fjord and the catchment area.

June, July, and August (JJA) satellite data were selected as the months with the most available supplementary data. Only images with more than 50% valid pixel observations were chosen for correlation analysis. For 2019, the year with available data from environmental variables, a linear model was developed for predictors of median $C_{SPM_{sat}}$ values and plume extent. Statistical analysis was performed on averaged values for satellite imagery (i.e., median values for $C_{SPM_{sat}}$ and river plume extent) and meteorological-environmental data from the weather- and river-monitoring stations. Therefore, the supplementary dataset based on the weather and environmental data was merged to the summary statistics per RS image based on the averaged values of environmental data over 24 h prior to the satellite observation. The following environmental predictors were tested against the log-transformed median values for $C_{SPM_{sat}}$ and river plumes extent for the datapoints in the JJA subset:

- Averaged air temperature (°C);
- Precipitation sums (mm);
- Averaged water level at the river station (m);
- Averaged turbidity T (NTU) at the river station.

Here, a combination of correlation matrix and regression analysis is used to determine relationships of environmental parameters and the evolution of SPM (concentration and river plume extent) in the fjord. All statistical analyses on extracted $C_{SPM_{sat}}$ and additional environmental datasets were performed in R 4.1.0 [71]. The functions "cor" (R basic package), and packages "corrplot" [75], and "reshape2" [76] were used for correlation analyses and to create elementary matrices, while "ggpmisc" [77] was used for the regressions and statistical evaluation of potential environmental predictors of SPM concentrations and plume extent in Adventfjorden. Both steps in the analysis were based on only complete observations. The packages "ggplot2" [78] and "RColorBrewer" [79] were used for arranging the data and visualization.

3. Results

3.1. Meteorological and Environmental Conditions in 2019 and 2020

Meteorologically, the year 2019 was colder and wetter than 2020, with average temperature and sum precipitation being −3.43 °C and 167 mm in 2019 and −3.38 °C and 137.9 mm in 2020, respectively (an overview of the meteorological conditions can be found in the Supplementary Figure S4). The average air temperature in JJA for 2019 was 6.46 °C, while in JJA 2020 it rose by 11.5% to an average of 7.2 °C. July 2020 also experienced an extreme heat event, with maximum air temperatures reaching higher than 20 °C for four consecutive days (25–29 July 2020). For both spring and autumn, precipitation and snow cover were strikingly higher 2019 compared to 2020. The lower air temperatures in winter and spring 2020 resulted in an exceptional sea-ice cover in the innermost parts of Adventfjorden, which was visible on satellite images until mid-May, whereas in 2019, sea ice was not observed in Adventfjorden (as is common for this fjord). Wind is a considerable factor in surface distribution of suspended and dissolved matter. Easterly and south-easterly

winds in Adventfjorden are predominant throughout the year and only disturbed by a period of westerly and south-westerly winds during the summer months (JJA).

3.2. In-Situ Measurements

SPM values presented an overall high variability in Adventfjorden in 2019 and 2020 ablation seasons (Table 1). In 2019, highest SPM values were found in early August, while in 2020, the values for SPM_{insitu} were particularly high in both June and July. It should be noted that the timing of the sampling in 2019 and 2020 is different, which will lead to differences in the measurements and subsequently monthly averaged values of particulate matter load in the fjord surface water.

Table 1. Summary of performed in-situ sampling during the 2019 and 2020 summer campaigns. Averaged values ($\pm$ SD) are given for suspended particulate matter (C_{SPM}), turbidity (T), and secchi depth (Z_{SD}) at n stations sampled. In 2020, turbidity was not measured.

Date	Platform	C_{SPM} $[\mathbf{mg\ L^{-1}}]$	T [**NTU**]	Z_{SD} [**m**]	n
14 June 2019	Basecamp	27.32 ± 7.5	19.50 ± 16.8	1.44 ± 1.32	11
17 June 2019	UNIS Kolga	25.73 ± 12.3	12.60 ± 11.98	1.01 ± 0.8	8
06 August 2019	UNIS Kolga	57.80 ± 24.13	40.53 ± 35.29	-	10
07 August 2019	UNIS Kolga	68.22 ± 56.34	19.30 ± 20.58	1.81 ± 1.72	8
12 June 2020	UNIS Polaris	115.45 ± 131.37	-	0.90 ± 1.31	11
17 July 2020	UNIS Polaris	70.41 ± 75.16	-	0.93 ± 1.03	11
30 July 2020	UNIS Polaris	156.68 ± 108.61	-	0.64 ± 0.75	9
26 August 2020	UNIS Polaris	28.01 ± 9.11	-	3.80 ± 2.04	10
22 September 2020	UNIS Kolga	7.32 ± 3.44	-	5.20 ± 1.59	11

The $C_{SPM_{insitu}}$ in Adventfjorden ranged from 4.7 to 152.36 mg L^{-1} and 3.57 to 434.95 mg L^{-1} in the studied years 2019 and 2020, respectively. In both years, the highest values for $C_{SPM_{insitu}}$ were found in the innermost stations of the fjord, with values ranging from 16.7 to 152.4 mg L^{-1} for the stations E1 and A1, A2, and A3, which were located within 1 km distance to the tidal flat of the estuary. The entry station of the river, E1, shows comparable values to the inner transect stations. The values for SPM_{insitu} generally decreased towards outer Adventfjorden. The lowest values for SPM were, thus, found at A6, the entry point to Isfjorden, with minimum of 4.7 mg L^{-1} $C_{SPM_{insitu}}$ over the course of both years. Turbidity was measured in the 2019 field campaigns only and followed largely the values of $C_{SPM_{insitu}}$. Averaged values and SD increased noticeably in August, illustrating the high variability seen in the values for C_{SPM}. Secchi depth Z_{SD} was measured as a solid indicator of photosynthetically available radiation within the water column. The negative non-linear relationship of Z_{SD} with $C_{SPM_{insitu}}$ is shown in the Supplementary Figure S3. Z_{SD} were shallowest during the June and July sampling days in 2020, with values as low as 0.05 m for the innermost station (A1) on 12 June 2020.

3.3. SPM Algorithm Calibration and Validation

Four match-up days of in-situ field measurements and clear-weather satellite images were achieved during the study period of 2019 and 2020 (Table 2, $n = 60$). However, only three dates were used: 14 June 2019, 06 August 2019, and 17 July 2020. The sampling day on the 30 July 2020 was classified as an outlier and removed due to the unique characteristics of the very high SPM load and turbidity likely caused by the extreme heatwave event (see above; an overview of the meteorological conditions is given in the Supplementary Figure S4). Quality assessment of the dataset revealed unusable data from two stations sampled on 06 August 2019. Subsequently, the remaining dataset ($n = 46$) was split based on values for $\rho_w(665)$ and $n = 23$ and $n = 23$ of $C_{SPM_{insitu}}$ paired with contemporaneous $\rho_w(665)$ values were used in the calibration/validation (cal/val) process, respectively.

Table 2. Overview of timing of sampling in Adventfjorden that coincided with the acquisition of the Sentinel-2 satellite imagery. Start and End time for field campaigns was taken from CTD casts and corrected for local time. The time (UTC) is given for every matchup date. Note that the cal/val data obtained on 30 July 2020 (in italic) was later excluded from the calibration.

Matchup Date	In-Situ Timing (UTC)		Sentinel-2 Acquisition (UTC)	
	Start	**End**	**S2A**	**S2B**
14 June 2019	10:48	13:18	12:57	12:06
06 August 2019	11:49	14:17	13:07	12:16
17 July 2020	11:14	13:46	–	12:37
30 July 2020	*11:03*	*14:23*	*11:58*	*12:47*

The results of the non-linear least squared regression analysis are presented in Table 3 (and visually in Figure 2) and include the results of the accuracy assessment based on the validation dataset. The A coefficient, essentially reflecting the backscattering characteristics of algal and non-algal particles was found to be higher and the C coefficient lower but within reasonable margins of the original calibration in Nechad et al. [41]. AdvFCal performed better on the validation dataset with MRD 47.5% and 29.1% for the Nechad- (NeCal) and the Adventfjorden calibration (AdvFCal), respectively. The calibrated algorithm also shows better values for RMSD and bias.

Table 3. Coefficients for the SPM-algorithm in the original (NeCal) [41] and the adapted regional (AdvFCal) calibration. Measures of accuracy are given with mean relative difference (MRD), root mean square difference (RMSD), bias, and the coefficient of determination (R^2).

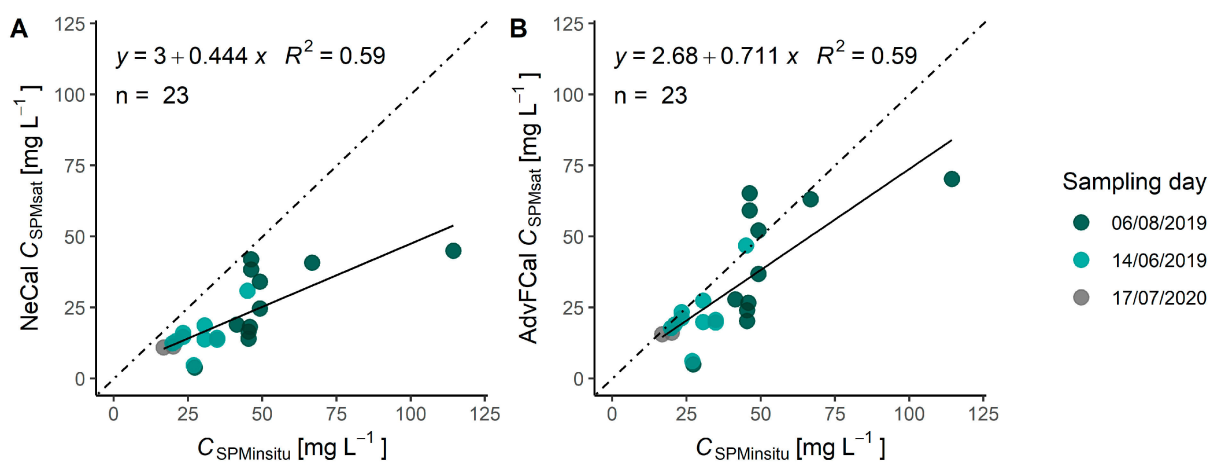|	Coefficients for $\rho_\mathbf{w}(665)$	MRD	RMSD	Bias	R^2
NeCal	A: 355.85, B: 1.74, C: 0.1728	47.5%	23.3%	−17.87	0.55
AdvFCal	A: 523.78, B: 1.97, C: 0.158	29.1%	15.9%	−7.72	0.55

Figure 2. Validation comparison of (**A**) the original SPM algorithm calibration (NeCal) and (**B**) the regionally tuned algorithm (AdvFCal) based on the match-up dataset from three sampling days, shown by the different colours. The dashed line illustrates a 1:1 relationship between modelled and in-situ values.

3.4. Sensitivity Analysis of AdvFCal

The visual validation (Figure 2) shows the underestimation of in-situ values in the NeCal calibration. While the retuned AdvFCal performs better, both calibrations show outliers for two match-up data points. Therefore, the sensitivity in the training data to different parameters was analysed. The sensitivity analysis on the cal/val dataset showed

marginal correlation between residuals of predicted and observed C_{SPM} values and the time-difference between the in-situ measurements and the satellite observation (Supplementary Figure S1). Additionally, we explored potential sensitivity to different concentrations of C_{SPM} and how it might affect the algorithm's performance. The use of different window sizes was explored (1×1, 3×3, 5×5 pixel) and showed negligible effects on residuals in the matchup dataset. Considering the very local processes in the estuary and the potential effects of pixel-mixing at the land-ocean interface, a high spatial resolution is needed [80]. We therefore processed the data at its native resolution of ~20 m.

3.5. Time-Series Analysis

A total of 116 Sentinel-2 (MSI) images were found to fit the criteria for the performed time-series analysis. The area of the polygon created as bounds for the satellite estimates over our AOI was ~29 km^2 (see Figure 1), consisting of more than 200.000 potential pixel estimates. In total, more than 15×10^6 valid pixel estimates could be yielded from the time-series dataset. For 2020, land-fast ice was still present in the inner parts of Adventfjorden, thus, limiting the number of valid retrievals in spring 2020 spatially to the mid-fjord and outer fjord regions and temporally to the time after the ice-breakup (around mid-May). Maps showing the valid observations per pixel can be found in the Supplementary Figure S2. The spatial resolution after processing was found to be ~20–27 m due to the specifications in the SeaDAS l2gen module.

The river plume extent exhibited a high degree of seasonal variability in both 2019 and 2020 (Figure 3). In both years the river plume extent remained well below 10% of the fjord area for most parts of the observation period, however, a strong increase in the plume extent was observed in mid-June, with values remaining elevated until late August both in 2019 and 2020. In 2019, the strong influence of the river plume began in mid-June (16 June 2019), when it increased from 5% to over 20% of the fjord over a two-day period. This increase also coincided with a 17 cm increase in river water level, observed at the river sensor station (marked in Figure 1). The maximum plume extent was 34.8% of the fjord area, on 09 July 2019, while the last observed day with significant plume extent in Adventfjorden was 06 August 2019. In 2020, the plume also developed toward mid-June, reaching 5.9% on the 17 June 2020. The maximum plume extent of 40.5% was observed between 26–27 July 2020, following the extreme heat event with very high (>20 °C) air temperatures for four consecutive days. Overall, the turbid plume in Adventfjorden does not exceed ~35% to ~41% of the total fjord area for 2019 and 2020, respectively. Noteworthily, the sampling days considered for the cal/val dataset coincided with the onset and offset of the plume influence in 2019, while the sampling campaigns were conducted during the time of enhanced riverine influence.

Variability between stations and years, observed in the in-situ measurements are reflected in the RS dataset. The RS data shows higher variability in the inner fjord stations for 2020 in contrast to 2019 (Figure 4). Generally, it is the inner fjord stations close to the Adventelva tidal flat that experience largest variability but also highest median $C_{SPM_{sat}}$ in both years. Reduced valid observations in early 2020 due to exceptional ice cover in Adventfjorden may lead to higher median values.
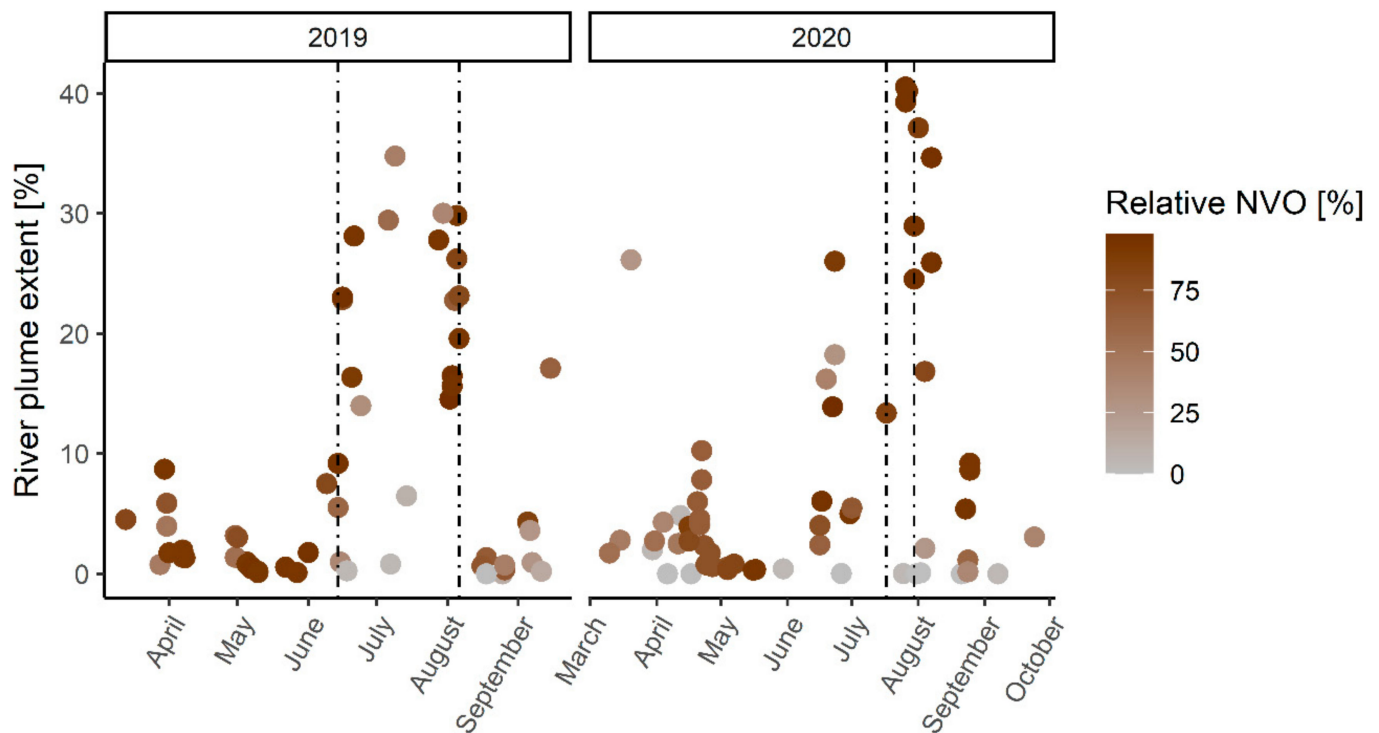
Figure 3. Relative area of Adventfjorden classified as river plume (i.e., covered by $C_{SPM_{sat}}$ values of 30 to 500 mg L^{-1}). Cloud cover as estimated from the relative number of valid observations (NVO) per day is shown as the gradient of colour. Images in JJA with extensive (>50%) cloud cover, i.e., invalid observations, were excluded from the environmental statistics later on. Dashed lines represent the in-situ matchup days considered for the cal/val dataset.
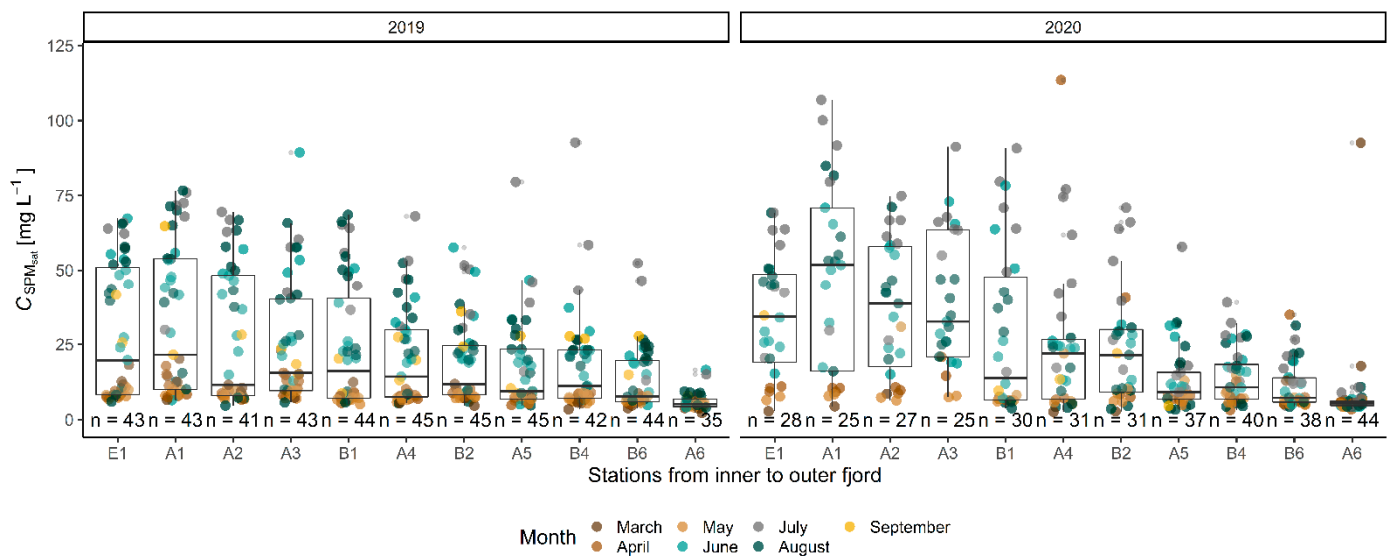

Figure 4. Box and whiskers plot with underlying point observations for $C_{SPM_{sat}}$ at the sampling stations in Adventfjorden in 2019 and 2020 (for FreshFate station grid see map in Figure 1). NVO (n) for each station are indicated below each boxplot. The stations are sorted from inner to outer fjord stations to illustrate spatial variability.

For the summer months (JJA), monthly composite pictures of $C_{SPM_{sat}}$ (calculated from averaged mean-values of $C_{SPM_{sat}}$) reveal strong differences in concentration and distribution of $C_{SPM_{sat}}$ between months (Figure 5). The maps show that the sediment-laden

water masses do not penetrate far out into the fjord in June, while for July the strong influence of SPM to nearly the whole surface area of Adventfjorden becomes apparent. $C_{\text{SPM}_{\text{sat}}}$ decreases significantly in August, leading to a characteristic threefold dynamic of SPM influence to Adventfjorden with strong gradients during the summer shoulder months June and August. Maps of binned monthly satellite images for JJA of coefficient of variation (CV) per pixel were chosen as an indicator of the spatial variability over time. Variability "hotspots" were mostly located in the very nearshore environments in Adventfjorden but are especially pronounced in the direct proximity of river outlets, such as Longyearelva or Hanaskogelva. Surprisingly, the CV values per pixel were less high in the tidal flat of Adventelva, indicating less pronounced changes over the monitoring period. Other areas of stronger variability appear to be the outlet in Hanaskogdalen on the northern side of Adventfjorden as well as the southwestern coast of Adventfjorden, where the data suggests influences from dispersed plumes from the close-by Bjørndalselva. Variability is generally higher in the middle parts of Adventfjorden in July compared to the other months.
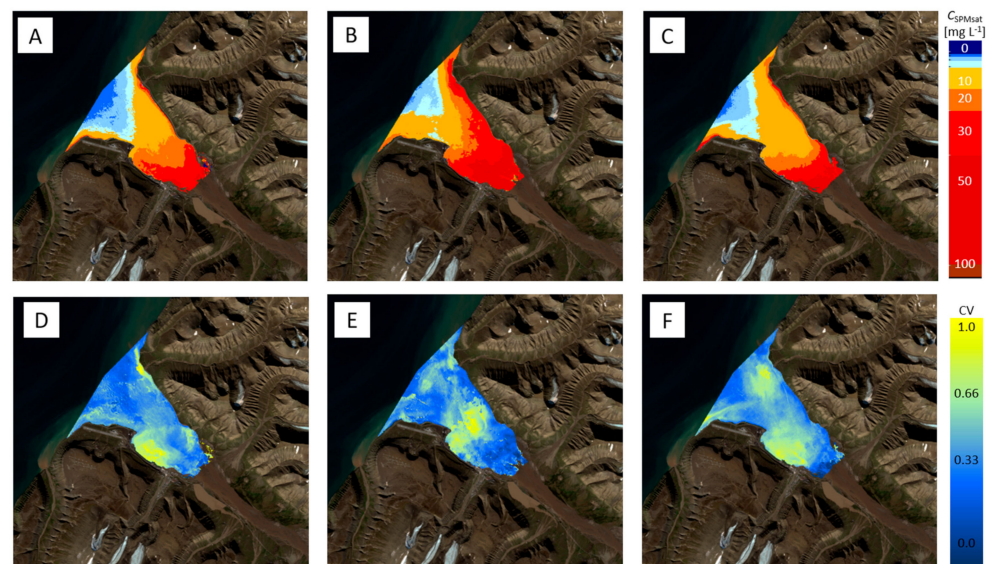
Figure 5. Composite images of mean values for $C_{\text{SPM}_{\text{sat}}}$ (upper panels) and coefficient of variation (CV, lower panel) per pixel during the months of June (**A**,**D**), July (**B**,**E**), and August (**C**,**F**). Composite are based on both 2019 and 2020 satellite imagery (background corresponding to Sentinel-2 image in overview map of this study). Contains modified Copernicus Sentinel-2 data (2020, Sentinel-2 B image 27 July 2020) processed by Sentinel-Hub (https://scihub.copernicus.eu/, accessed on 28 June 2021).

3.6. Environmental Statistics

Pearson correlation analysis was performed on the JJA 2019 subset to the dataset (n = 21). The strongest relationship defined by the Pearson correlation coefficient r was found between the median $logC_{\text{SPM}_{\text{sat}}}$ values and the river water level over the previous 24 h (r = 0.89, p < 0.005) or the river plume extent ($C_{\text{SPM}_{\text{sat}}}$>30 mg L^{-1}) and the air temperature during the previous 24 h (r = 0.78, p < 0.005). Since air temperature data was available for the analysis of the 2020 dataset as well, we can show that the relationship persisted over the whole dataset, increasing the correlation to r = 0.83. An overview is given in the correlation plot in the Supplementary Figure S5. Linear models for the above-mentioned predictors of median $C_{\text{SPM}_{\text{sat}}}$ and plume extent confirmed the high explanatory power of the tested environmental parameters with R^2 (coefficient of determination) being 0.69 for the relationship of averaged air temperature and the relative cover of the fjord by plume (Figure 6).
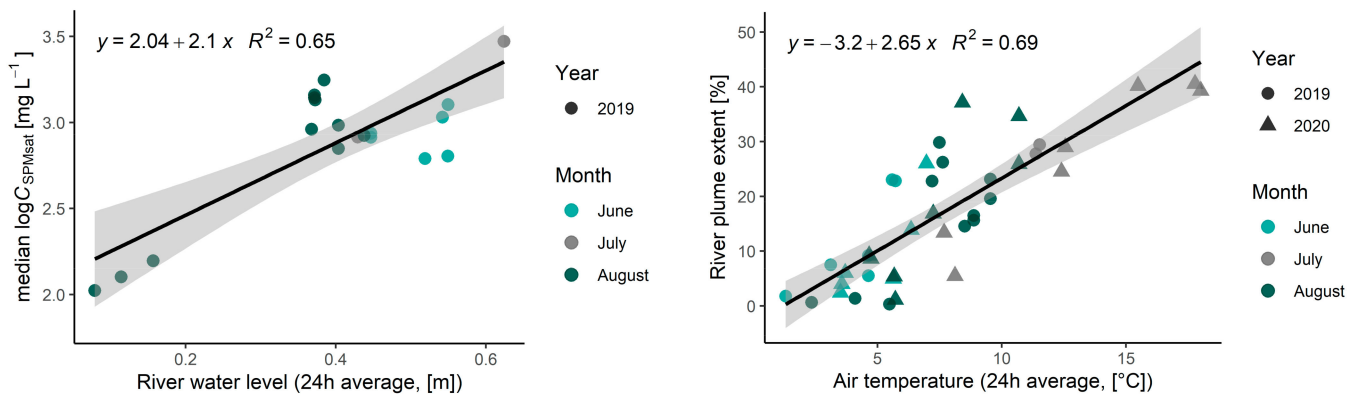
Figure 6. Linear model showing the analysed relationship of the satellite derived river plume extent ($C_{SPM_{sat}} > 30$ mg L^{-1}) and air temperature (°C) as well as the river water level and median values of $logC_{SPM}$. The equation and R^2, the coefficient of determination, are given. Colours and shapes represent the month and year of the satellite acquisition, respectively.

4. Discussion

This study proposed a regionally calibrated algorithm (AdvFCal) based on the well-established NeCal by Nechad et al. [41]. We show that regional or site-specific tuning is crucial, especially in complex nearshore environments [35], as it enhanced the accuracy of satellite-derived time-series analysis of $C_{SPM_{sat}}$ by ~20% for the targeted study region. The yielded RS dataset covered two complete summer seasons in 2019 and 2020 and managed in a satisfactory way to detect the onset and length of the runoff season from satellite imagery based on the distinct change in the freshwater-driven $C_{SPM_{sat}}$. With the ~20 m spatial resolution achieved in our workflow on S2 data, trends in riverine inputs to the dynamic and complex nearshore zones of inaccessible Arctic fjords can be explored. Especially during the summer months, the extensive time-series dataset allows a near-daily monitoring of river plume evolution and has the potential to monitor the long-term trends, such as coastal darkening and related decrease of benthic light availability [22]. It is reasonable to believe that the calibration holds for comparable catchments in polar regions, dominated by glaciogenic sediments. Indeed, a comparable study showed a solid reliability for the transfer of a regionally tuned turbidity algorithm [35], which may indicate the broader applicability of the calibration AdvFCal to a wider spectrum of Arctic coasts.

4.1. Surface Water SPM Exhibits High Variability in Space and Time

The particle load in the surface water in Adventfjorden showed considerable spatial differences within the in-situ data, and also within the spatially more-comprehensive RS dataset (see also Figures 3–5). The concentration and distribution of SPM varied strongly during the studied period with persistently high values found in the summer months of June, July, and August of 2019 and 2020, respectively. The estimated values for C_{SPM} (both in-situ and from OCRS) are consistent with earlier studies from Zajączkowski [49] and Weslawski [48], with 112 mg L^{-1} and 200–500 mg L^{-1}, respectively. The range of values for SPM was naturally found to be particularly high in the inner fjord stations, in accordance with previous in-situ studies [24,48,56,81]. The spatial distribution of sediment-laden water masses seems to be most commonly observed as a deflection to the right of the river mouth, following the Coriolis force [8,15].

We were able to extract the coefficient of variation (CV) per pixel to describe the most variable locations of surface C_{SPM} in Adventfjorden (Figure 5). We see CV increasing during the summer months (JJA), especially close to river outlets from catchments with steeper terrain. The river outlet of Longyearelva is, in our dataset, a striking source of variability compared to the wider Adventelva river outlet. The longer passage of discharged glacial meltwater through the valley of Adventdalen might offer a possible explanation, as particles will have the time to settle and accumulate in river channels [82]. In contrast, glaciers in

Longyeardalen [83] as well as the steeper catchment terrain may support higher discharge velocities with subsequent effects on SPM concentration and variability. In our data, the considerably higher water levels in 2020 measured at the river monitoring station may be relatable to Longyearelva and explain the generally higher values of SPM load during JJA 2020. Areas of high variability will favour a community structure that is adapted to a wider range of physico-chemical properties. Identification of hotspots of variability through binned satellite imagery might deliver a crucial metric for ecosystem studies targeting community structure or shifts in productivity.

A study on subglacial discharge in Raudvika in Kongsfjorden, Svalbard, found C_{SPM} ranging as high as 600 mg L^{-1} at the glacier front using Landsat-8 imagery and a band-ratio algorithm [84]. The direct discharge of turbid subglacial meltwater enriched with inorganic particles may, however, only compare to a certain degree to the retention potential of extensive river valleys that drain a comparably large area that is under various influences. This may also be evident in the differences in suspended particle load in subpolar fjord systems such as the Norwegian Trondheimsfjord and Sognefjord, where values for suspended matter were substantially lower (maximal C_{SPM} 1.40 and 2.23 mg L^{-1}, respectively) [10]. Here, not only catchment size but also the presence of vegetation in the river valley may be a reasonable explanation for the observed differences, as longer retention times and disturbance by vegetation may prevent sediments from mobilising to the same degree and cause sediments and particles to settle more readily.

Arctic coastal zones and fjords off Svalbard generally exhibit comparably lower C_{SPM}. In the case of several studies in Greenland [19,28,85], C_{SPM} estimated mainly from in-situ measurements were typically a fractional amount (~10%) of the values observed in Adventfjorden. When comparing these values, it is, however, important to acknowledge the differences in study design as well as the characteristics of the fjord or estuary studied. The length of most of the other Arctic study areas encompassed longer distances, leading to more sediment loss over longer distances from the river mouth or glacier front, which subsequently might explain lower median values. In the case of the Uummannaq fjord and Vaigat-Disko bay [19], the length of both fjords is tenfold that of Adventfjorden.

4.2. Temperature Drives Mobilisation and Transport of SPM to Arctic Fjords

The values of averaged air temperature 24 h prior to the observation showed a strong (r = 0.83, R^2 = 0.69) correlation with the river plume extent and a less pronounced, yet significant relationship, with the median of log-transformed $C_{SPM_{sat}}$ values (r = 0.59). This might illustrate how dilution of particles during times of higher discharge can foster a larger extent of the plume itself while C_{SPM} might not grow proportionally. Mobilisation of particles from subglacial discharge and erosion processes in the catchment are generally tied to discharged volume and velocity of water flow in the catchment [54].

The here-presented satellite-based dataset could not support a strong relationship of either median values of $C_{SPM_{sat}}$ or the river plume extent ($C_{SPM_{sat}}$> 30 mg L^{-1}) to the precipitation values in the previous 24 h—a relationship discussed in other publications (e.g., [86]). However, continuous rainfall over longer periods of time as well as extreme rainfall events will sustain higher water levels in the rivers and have subsequent effects on particle fluxes from mobilised sediments. In fact, air temperature was reported to be the more significant predictor in the first half of the runoff season [86], while during the second half, the effects of rainfall events have been found to be more pronounced in an upstream transect in Adventelva [82]. From lack of valid RS observations in late August and September, paired with our own on-ground observations of the occurrence of a substantial river plume after rainfall events, we conclude that the RS-based analysis might underestimate the importance of precipitation-driven riverine impacts on Adventfjorden during late summer and early autumn.

The results are evidence that supports the mobilisation potential with increasing temperatures (both during the ablation season as well as over longer time scales) but it should be noted that these results cannot exclude the influence of additional and/or

connected environmental drivers. The generalization of presented results on other fjords should be critically reviewed as strong regionality and complex interplay of influencing factors may apply. However, predicting ecologically important endpoints such as river plume extent and SPM concentration in productive systems, such as fjords, from elementary environmental data (i.e., air temperature) highlights the exceptional value of combinations of OCRS in combination with extensive time-series data on environmental conditions.

4.3. Ecological Implications under Climate Change

Warming temperatures will affect the length of the ablation season in high latitude and Arctic regions, leading to enhanced melt of snow and ice. This might in turn fuel longer runoff seasons and subsequent mobilisation of sediments. In fact, recent studies suggest a general retreat for most glaciers and negative mass balances on the Svalbard archipelago: simulations based on Representative Concentration Pathways (RCP) 4.5 and 8.5 used by van Pelt et al. [4] found highest glacial retreat probability for the southern part of Spitsbergen, due to increase in runoff from both glaciers and land. Nowak et al. [2] come to a comparable conclusion, while acknowledging that "peak water" (i.e., a levelling-off in runoff values [87]) is likely to happen if catchment potential is exhausted. Nonetheless, major changes to the glacial landscape in Svalbard are happening, causing the retreat of previously marine-terminating glacier fronts to move further inland [88] with implications for the hydrological and sedimentary characteristics in the transition zones from land to sea. Indeed, primary productivity is significantly different for marine-terminating and land-terminating glaciers [89,90]. While the upwelling by subglacial discharge at the marine terminus delivers essential nutrients to the surface waters [89,91,92], non-glaciated fjords will feature strong freshwater-driven stratification and enhanced turbidity, restraining the majority of primary productivity and subsequent carbon fixation to surface waters [85]. We therefore propose that Adventfjorden may represent a model environment of "post-glaciation" (i.e., deglaciated) estuaries beyond the limits of the Svalbard archipelago.

The strong relationship observed between $C_{SPM_{sat}}$ and Z_{SD} (Supplementary Figure S3) highlights the role of turbid river plumes in driving high light attenuation and thereby reducing coastal light availability [17]. The presence of turbid freshwater plumes negatively impacts the productivity of primary producers in the nearshore zone by reducing the light availability in the water column. In these deglaciated and (mostly) ice-free Arctic fjords, light attenuation driven by high concentrations of suspended matter become a considerable force in structuring the phenology of primary production and carbon uptake [17,19]. High values of SPM (higher than 30 mg L^{-1}) in this study have been found to be limiting the illumination by incident light to the uppermost 50 cm in most cases (based on the Z_{SD} and $C_{SPM_{insitu}}$ dataset). The erosion potential of the catchment was not considered in this study but could allow the evaluation of C_{SPM}, which would in turn lead to a better understanding of the vulnerability of these coastal environments due to enhanced particle transport in glaciated catchments and turbidity fluxes in the productive nearshore zone. Further investigation, drawing on available and additional data on SPM, Chl-a, CDOM and other OACs may be necessary to fully understand the dynamics. OCRS techniques may provide a larger spatial understanding of optical water properties driven by these parameters. The application of regionally adapted OCRS algorithms, especially in remote but productive Arctic coastal environments, has the potential to detect changes to the light availability and may offer the opportunity to develop an optical classification of the water column [93]. This study has targeted the prevailing concentrations of suspended particles, however, dissolved organic and inorganic matter (CDOM) can contribute largely to the absorption and benthic light availability [10]. There is a large potential in resolving the complexity in the chemical physicochemical composition of optically active constituents to describe the variability of coastal marine ecosystems.

4.4. Potential for Remote and Satellite Observations of SPM in Arctic Fjord Estuaries

The use of OCRS fills gaps in our understanding of variability of ecologically relevant water quality parameters, such as SPM, which has been targeted in this study. The hereby proposed use of $C_{\text{SPM}_{\text{sat}}}$ analysis from high resolution satellite data can provide a necessary metric to model changes to the water level by providing a strong relationship between the satellite detected median $C_{\text{SPM}_{\text{sat}}}$ over Adventfjorden and river water level in Adventelva. In contrast to in-situ-based studies, this OCRS-based approach can resolve SPM variability at unprecedented frequency and spatial scale. Regional tuning of an existing algorithm was necessary to enhance the quality of satellite-derived C_{SPM}. Certain limitations of this approach became, however, apparent and should be addressed in further studies.

In our study, we found the performance for the regional calibration AdvFCal based on the Nechad et al. [41] algorithm to not fully detect the highest values of SPM in the nearshore zone. The lack of calibration and ground-truthing data for outer fjord stations with lower concentrations of SPM was most likely responsible for the larger offset values in the regional calibrated AdvFCal algorithm in this study, which caused a general overestimation of SPM values in clearer outer fjord waters. Furthermore, the generality of SPM detection through OCRS might be constrained by a limited range of values that can be modelled by semi-analytical algorithms with certainty [42]. In this study, a single-band approach delivered satisfactory results. However, the quantification of pixel-values, especially for high to extremely high C_{SPM} can likely be improved using switching algorithms [47,94]. Especially in regions with higher fluxes in allochthonous sediments and less primary productivity, the accuracy in otherwise underestimated C_{SPM} values > 60 mg L^{-1} could be enhanced. For the purpose of detecting a threshold value as used in this study based on ecologically meaningful 30 mg L^{-1} C_{SPM}, this approach allowed for the very detailed discussion of the variability of turbid plumes in the Arctic fjord of Adventfjorden within margins of acceptable uncertainty of less than 30% [65,95].

The IOPs of SPM may not always correspond well to the signal that is recorded by the satellite. In fact, the optical properties of SPM change with the particle mass, size, and density [96]. In the Adventfjorden system, there are also likely to be strong seasonal changes [12,83] which influence SPM composition and optical properties (e.g., with higher inorganic content during periods with high contributions of glacial-meltwater [32], and higher organic content during later summer rainfall events when the permafrost active layer is deeper [12,97]). We therefore suggest that monthly or seasonal calibrations to model C_{SPM} could provide better predictive power, as proposed by [98] for the Baltic Sea region.

We propose the use of the system of the Sentinel-2 mission for monitoring purposes at high to medium resolution. However, there are obvious limitations to optical satellite sensors regarding cloud cover or spatial resolution. Drone-based surveying of complex nearshore waters should therefore be considered [34]. They can complement satellite observations while being currently limited in their spatial coverage and revisit time. In the case of monitoring of Arctic nearshore waters in Svalbard, the recently launched hyperspectral sensor on board the Dornier small-wing plan stationed in Longyearbyen may prove a necessary and useful addition, especially during the cloudier summer season [99]. These high-resolution sensors may, however, be more adequate for targeted surveying while continuous monitoring can build on the temporal resolution of satellite data.

5. Conclusions

This study explored the fluxes of SPM into an Arctic fjord-type estuary over the course of two runoff seasons in 2019 and 2020 on a spatially and temporally improved dataset by using in-situ observations to calibrate a generic semi-analytical algorithm from Nechad et al. [41]. We located variability "hotspots" for SPM at the more channelled riverine entry points, of, e.g., Longyearelva, to the fjord, while values were more stable in the tidal flat of Adventelva, indicating the effects of catchment topography on the velocity of the runoff throughout the season and the potential for particle mobilisation. Combining the time-series data with environmental driver data, we identified ambient

air temperature (°C) as a predictor to the elevated C_{SPM} and its spatial coverage in the fjord, supporting the well-reported effects of temperature on glacial discharge and the mobilisation of terrestrial particulate matter. This highlights the explanatory power of OCRS combined with environmental data in these dynamic environments.

The recorded and ongoing changes to temperature in the Arctic will likely change the phenology and variability of light attenuating SPM in near-shore regions and fjords. This study suggests that the Adventfjorden estuary can function as a valid model area for regions that are presently governed by marine terminating glaciers and predominantly glaciated catchments. Fine-tuning of the OCRS algorithms by in-situ measurements led to acceptable estimates of spatio-temporal variability of SPM in the highly dynamic Adventfjorden estuary and, thus, closes knowledge gaps related to more snapshot-like in-situ observations of optically active water constituents, specifically for SPM. This is a substantial improvement to previous study designs in the area that were either based on in-situ observations or could not provide a comparable resolution of RS based estimation. To improve the accuracy even more, longer time series of cal/val and matchup datasets may be required, covering clearer water in the outer fjord stations to complex turbid waters in the inner parts of the fjord equally. With the seasonality in runoff and SPM concentration in the surface waters of fjordic estuaries, such as the here-studied Adventfjorden, serious consideration should be given to seasonally tuned calibrations. The here-presented results highlight the use of remote sensing data for the monitoring purposes of complex Arctic coasts.

References

1. Hanssen-Bauer, I.; Førland, E.; Hisdal, H.; Mayer, S.; Sandø, A.B.; Sorteberg, A. (Eds.) *Climate in Svalbard 2100: A Knowledge Base for Climate Adaptation*; NCCS Report No. 1/2019; NCCS: Albuquerque, NM, USA, 2019.
2. Nowak, A.; Hodgkins, R.; Nikulina, A.; Osuch, M.; Wawrzyniak, T.; Kavan, J.; Łepkowska, E.; Majerska, M.; Romashova, K.; Vasilevich, I.; et al. *From Land to Fjords: The Review of Svalbard Hydrology from 1970 to 2019 (SvalHydro)*; Loughborough University: Loughborough, UK, 2021.
3. IPCC. *IPCC Special Report on the Ocean and Cryosphere in a Changing Climate*; Pörtner, H.-O., Roberts, D.C., Masson-Delmotte, V., Zhai, P., Tignor, M., Poloczanska, E., Mintenbeck, K., Alegría, A., Nicolai, M., Okem, A., et al., Eds.; Summary for policy makers; IPCC: Geneva, Switzerland, 2019.
4. van Pelt, W.J.J.; Schuler, T.V.; Pohjola, V.A.; Pettersson, R. Accelerating future mass loss of Svalbard glaciers from a multi-model ensemble. *J. Glaciol.* **2021**, *67*, 485–499. [CrossRef]
5. Lantuit, H.; Overduin, P.P.; Couture, N.; Wetterich, S.; Aré, F.; Atkinson, D.; Brown, J.; Cherkashov, G.; Drozdov, D.; Forbes, D.L.; et al. The Arctic Coastal Dynamics Database: A New Classification Scheme and Statistics on Arctic Permafrost Coastlines. *Estuaries Coasts* **2012**, *35*, 383–400. [CrossRef]
6. Vonk, J.E.; Tank, S.E.; Bowden, W.B.; Laurion, I.; Vincent, W.F.; Alekseychik, P.; Amyot, M.; Billet, M.F.; Canário, J.; Cory, R.M.; et al. Reviews and syntheses: Effects of permafrost thaw on Arctic aquatic ecosystems. *Biogeosciences* **2015**, *12*, 7129–7167. [CrossRef]
7. Cottier, F.R.; Nilsen, F.; Skogseth, R.; Tverberg, V.; Skarðhamar, J.; Svendsen, H. Arctic fjords: A review of the oceanographic environment and dominant physical processes. *Geol. Soc. Lond. Spec. Publ.* **2010**, *344*, 35–50. [CrossRef]
8. Syvitski, J.P.M.; Burrell, D.C.; Skei, J.M. *Fjords: Processes and Products*; Springer: New York, NY, USA; London, UK, 1987; ISBN 0-387-96342-1.
9. Lund-Hansen, L.C.; Andersen, T.J.; Nielsen, M.H.; Pejrup, M. Suspended Matter, Chl-a, CDOM, Grain Sizes, and Optical Properties in the Arctic Fjord-Type Estuary, Kangerlussuaq, West Greenland during Summer. *Estuaries Coasts* **2010**, *33*, 1442–1451. [CrossRef]
10. Mascarenhas, V.J.; Voß, D.; Wollschlaeger, J.; Zielinski, O. Fjord light regime: Bio-optical variability, absorption budget, and hyperspectral light availability in Sognefjord and Trondheimsfjord, Norway. *J. Geophys. Res. Oceans* **2017**, *122*, 3828–3847. [CrossRef]
11. Terhaar, J.; Lauerwald, R.; Regnier, P.; Gruber, N.; Bopp, L. Around one third of current Arctic Ocean primary production sustained by rivers and coastal erosion. *Nat. Commun.* **2021**, *12*, 169. [CrossRef]
12. McGovern; MPavlov, A.K.; Deininger, A.; Granskog, M.A.; Leu, E.; Søreide, J.E.; Poste, A.E. Terrestrial Inputs Drive Seasonality in Organic Matter and Nutrient Biogeochemistry in a High Arctic Fjord System (Isfjorden, Svalbard). *Front. Mar. Sci.* **2020**, *7*. [CrossRef]
13. Wolanski, E. *Estuarine Ecohydrology*, 1st ed.; Elsevier: Amsterdam, The Netherlands, 2007; ISBN 978-0-444-530660.
14. Mann, K.H. *Ecology of Coastal Waters: With Implications for Management*, 2nd ed.; Blackwell Science: Malden, MA, USA, 2000; ISBN 0-86542-550-7.
15. Forwick, M.; Vorren, T.O.; Hald, M.; Korsun, S.; Roh, Y.; Vogt, C.; Yoo, K.-C. Spatial and temporal influence of glaciers and rivers on the sedimentary environment in Sassenfjorden and Tempelfjorden, Spitsbergen. *Geol. Soc. Lond. Spec. Publ.* **2010**, *344*, 163–193. [CrossRef]
16. Bianchi, T.S.; Arndt, S.; Austin, W.E.; Benn, D.I.; Bertrand, S.; Cui, X.; Faust, J.C.; Koziorowska-Makuch, K.; Moy, C.M.; Savage, C.; et al. Fjords as Aquatic Critical Zones (ACZs). *Earth-Sci. Rev.* **2020**, *203*, 103145. [CrossRef]
17. Pavlov, A.K. The Underwater Light Climate in Kongsfjorden and Its Ecological Implications. In *The Ecosystem of Kongsfjorden, Svalbard*; Hop, H., Wiencke, C., Eds.; Springer: Cham, Switzerland, 2019; ISBN 978-3-319-46425-1.
18. Kirk, J.T.O. *Light and Photosynthesis in Aquatic Ecosystems*; Cambridge University Press: Cambridge, UK, 2010; ISBN 9781139168212.
19. Holinde, L.; Zielinski, O. Bio-optical characterization and light availability parameterization in Uummannaq Fjord and Vaigat–Disko Bay (West Greenland). *Ocean Sci.* **2016**, *12*, 117–128. [CrossRef]
20. Frigstad, H.; Kaste, Ø.; Deininger, A.; Kvalsund, K.; Christensen, G.; Bellerby, R.G.J.; Sørensen, K.; Norli, M.; King, A.L. Influence of Riverine Input on Norwegian Coastal Systems. *Front. Mar. Sci.* **2020**, *7*. [CrossRef]
21. Aksnes, D.L.; Dupont, N.; Staby, A.; Fiksen, Ø.; Kaartvedt, S.; Aure, J. Coastal water darkening and implications for mesopelagic regime shifts in Norwegian fjords. *Mar. Ecol. Prog. Ser.* **2009**, *387*, 39–49. [CrossRef]

22. Konik, M.; Darecki, M.; Pavlov, A.K.; Sagan, S.; Kowalczuk, P. Darkening of the Svalbard Fjords Waters Observed With Satellite Ocean Color Imagery in 1997–2019. *Front. Mar. Sci.* **2021**, *8*. [CrossRef]

23. Neukermans, G.; Ruddick, K.; Loisel, H.; Roose, P. Optimization and quality control of suspended particulate matter concentration measurement using turbidity measurements. *Limnol. Oceanogr. Methods* **2012**, *10*, 1011–1023. [CrossRef]

24. Elverhøi, A.; Lønne, Ø.; Seland, R. Glaciomarine sedimentation in a modern fjord environment, Spitsbergen. *Polar Res.* **1983**, *1*, 127–149. [CrossRef]

25. IOCCG. *Earth Observations in Support of Global Water Quality Monitoring*; Greb, S., Dekker, A., Binding, C., Eds.; IOCCG Report Series, No. 17; IOCCG: Dartmouth, NS, Canada, 2018.

26. Doxaran, D.; Ehn, J.; Bélanger, S.; Matsuoka, A.; Hooker, S.; Babin, M. Optical characterisation of suspended particles in the Mackenzie River plume (Canadian Arctic Ocean) and implications for ocean colour remote sensing. *Biogeosciences* **2012**, *9*, 3213–3229. [CrossRef]

27. Ehn, J.K.; Reynolds, R.A.; Stramski, D.; Doxaran, D.; Lansard, B.; Babin, M. Patterns of suspended particulate matter across the continental margin in the Canadian Beaufort Sea during summer. *Biogeosciences* **2019**, *16*, 1583–1605. [CrossRef]

28. McGrath, D.; Steffen, K.; Overeem, I.; Mernild, S.H.; Hasholt, B.; van den Broeke, M. Sediment plumes as a proxy for local ice-sheet runoff in Kangerlussuaq Fjord, West Greenland. *J. Glaciol.* **2010**, *56*, 813–821. [CrossRef]

29. Klein, K.P.; Lantuit, H.; Heim, B.; Fell, F.; Doxaran, D.; Irrgang, A.M. Long-Term High-Resolution Sediment and Sea Surface Temperature Spatial Patterns in Arctic Nearshore Waters Retrieved Using 30-Year Landsat Archive Imagery. *Remote Sens.* **2019**, *11*, 2791. [CrossRef]

30. Groom, S.; Sathyendranath, S.; Ban, Y.; Bernard, S.; Brewin, R.; Brotas, V.; Brockmann, C.; Chauhan, P.; Choi, J.; Chuprin, A.; et al. Satellite Ocean Colour: Current Status and Future Perspective. *Front. Mar. Sci.* **2019**, *6*, 28. [CrossRef]

31. Neder, C.; Fofonova, V.; Androsov, A.; Kuznetsov, I.; Abele, D.; Falk, U.; Schloss, I.R.; Sahade, R.; Jerosch, K. Modelling suspended particulate matter dynamics at an Antarctic fjord impacted by glacier melt. *J. Mar. Syst.* **2022**, *231*, 103734. [CrossRef]

32. Moskalik, M.; Ćwiąkała, J.; Szczuciński, W.; Dominiczak, A.; Głowacki, O.; Wojtysiak, K.; Zagórski, P. Spatiotemporal changes in the concentration and composition of suspended particulate matter in front of Hansbreen, a tidewater glacier in Svalbard. *Oceanologia* **2018**, *60*, 446–463. [CrossRef]

33. Melton, S.M.; Alley, R.B.; Anandakrishnan, S.; Parizek, B.R.; Shahin, M.G.; Stearns, L.A.; LeWinter, A.L.; Finnegan, D.C. Meltwater drainage and iceberg calving observed in high-spatiotemporal resolution at Helheim Glacier, Greenland. *J. Glaciol.* **2022**, 1–17. [CrossRef]

34. Wójcik, K.A.; Bialik, R.J.; Osińska, M.; Figielski, M. Investigation of Sediment-Rich Glacial Meltwater Plumes Using a High-Resolution Multispectral Sensor Mounted on an Unmanned Aerial Vehicle. *Water* **2019**, *11*, 2405. [CrossRef]

35. Klein, K.P.; Lantuit, H.; Heim, B.; Doxaran, D.; Juhls, B.; Nitze, I.; Walch, D.; Poste, A.; Søreide, J.E. The Arctic Nearshore Turbidity Algorithm (ANTA) - A multi sensor turbidity algorithm for Arctic nearshore environments. *Sci. Remote Sens.* **2021**, *4*, 100036. [CrossRef]

36. Petit, T.; Hamre, B.; Sandven, H.; Röttgers, R.; Kowalczuk, P.; Zablocka, M.; Granskog, M.A. Inherent optical properties of dissolved and particulate matter in an Arctic fjord (Storfjorden, Svalbard) in early summer. *Ocean Sci.* **2022**, *18*, 455–468. [CrossRef]

37. Slonecker, E.T.; Jones, D.K.; Pellerin, B.A. The new Landsat 8 potential for remote sensing of colored dissolved organic matter (CDOM). *Mar. Pollut. Bull.* **2016**, *107*, 518–527. [CrossRef]

38. IOCCG. *Ocean Colour Remote Sensing in Polar Seas*; Babin, M., Arrigo, K., Bélanger, S., Forget, M.-H., Eds.; IOCCG Report Series, No. 16; IOCCG: Dartmouth, NS, Canada, 2015.

39. Bélanger, S.; Babin, M.; Tremblay, J.-É. Increasing cloudiness in Arctic damps the increase in phytoplankton primary production due to sea ice receding. *Biogeosciences* **2013**, *10*, 4087–4101. [CrossRef]

40. Dogliotti, A.I.; Ruddick, K.G.; Nechad, B.; Doxaran, D.; Knaeps, E. A single algorithm to retrieve turbidity from remotely-sensed data in all coastal and estuarine waters. *Remote Sens. Environ.* **2015**, *156*, 157–168. [CrossRef]

41. Nechad, B.; Ruddick, K.G.; Park, Y. Calibration and validation of a generic multisensor algorithm for mapping of total suspended matter in turbid waters. *Remote Sens. Environ.* **2010**, *114*, 854–866. [CrossRef]

42. Han, B.; Loisel, H.; Vantrepotte, V.; Mériaux, X.; Bryère, P.; Ouillon, S.; Dessailly, D.; Xing, Q.; Zhu, J. Development of a Semi-Analytical Algorithm for the Retrieval of Suspended Particulate Matter from Remote Sensing over Clear to Very Turbid Waters. *Remote Sens.* **2016**, *8*, 211. [CrossRef]

43. IOCCG. *Synergy between Ocean Colour and Biogeochemical/Ecosystem Models*; Dutkiewicz, S., Ed.; IOCCG Report Series, No. 19; IOCCG: Dartmouth, NS, Canada, 2020.

44. Matthews, M.W. A current review of empirical procedures of remote sensing in inland and near-coastal transitional waters. *Int. J. Remote Sens.* **2011**, *32*, 6855–6899. [CrossRef]

45. Shanmugam, P.; He, X.; Singh, R.K.; Varunan, T. A modern robust approach to remotely estimate chlorophyll in coastal and inland zones. *Adv. Space Res.* **2018**, *61*, 2491–2509. [CrossRef]

46. Novoa, S.; Doxaran, D.; Ody, A.; Vanhellemont, Q.; Lafon, V.; Lubac, B.; Gernez, P. Atmospheric Corrections and Multi-Conditional Algorithm for Multi-Sensor Remote Sensing of Suspended Particulate Matter in Low-to-High Turbidity Levels Coastal Waters. *Remote Sens.* **2017**, *9*, 61. [CrossRef]

47. Ody, A.; Doxaran, D.; Verney, R.; Bourrin, F.; Morin, G.P.; Pairaud, I.; Gangloff, A. Ocean Color Remote Sensing of Suspended Sediments along a Continuum from Rivers to River Plumes: Concentration, Transport, Fluxes and Dynamics. *Remote Sens.* **2022**, *14*, 2026. [CrossRef]

48. Weslawski, J. Influence of salinity and suspended matter on benthos of an Arctic tidal flat. *ICES J. Mar. Sci.* **1999**, *56*, 194–202. [CrossRef]

49. Zajączkowski, M. Sediment supply and fluxes in glacial and outwash fjords, Kongsfjorden and Adventfjorden, Svalbard. *Pol. Polar Res.* **2008**, *29*, 59–72.

50. Norwegian Polar Institute. *Kartdata Svalbard 1:100 000 (S100 Kartdata)/Map Data*; Norwegian Polar Institute: Tromsø, Norway, 2014. [CrossRef]

51. Kartverket—Norwegian Mapping Authority. Sjøkart—Dybdedata. Available online: https://kartkatalog.geonorge.no/metadata/kartverket/dybdedata/2751aacf-5472-4850-a208-3532a51c529a (accessed on 30 January 2022).

52. Zajączkowski, M.; Szczuciński, W.; Bojanowski, R. Recent changes in sediment accumulation rates in Adventfjorden, Svalbard. *Oceanologia* **2004**, *46*, 217–231.

53. Hagen, J.O.; Lisestøl, O.; Erik, R.; Jørgensen, T. *Glacier Atlas of Svalbard and Jan Mayen*; Meddelelser No. 129; Norsk Polarinstitutt: Oslo, Norway, 1993; Available online: https://brage.npolar.no/npolar-xmlui/handle/11250/173065 (accessed on 18 April 2022).

54. Bogen, J.; Bønsnes, T.E. Erosion and sediment transport in High Arctic rivers, Svalbard. *Polar Res.* **2003**, *22*, 175–189. [CrossRef]

55. Węsławski, J.M. *Adventfjorden: Arctic Sea in the Backyard*; Institute of Oceanology PAS: Sopot, Poland, 2011.

56. Zajączkowski, M.; Nygård, H.; Hegseth, E.N.; Berge, J. Vertical flux of particulate matter in an Arctic fjord: The case of lack of the sea-ice cover in Adventfjorden 2006–2007. *Polar Biol.* **2010**, *33*, 223–239. [CrossRef]

57. Wiedmann, I.; Reigstad, M.; Marquardt, M.; Vader, A.; Gabrielsen, T.M. Seasonality of vertical flux and sinking particle characteristics in an ice-free high arctic fjord—Different from subarctic fjords? *J. Mar. Syst.* **2016**, *154*, 192–205. [CrossRef]

58. *ISO 11923:1997*; Water Quality—Determination of Suspended Solids by Filtration through Glass-Fibre Filters. ISO: Geneva, Switzerland, 1997. Available online: https://www.iso.org/standard/20654.html (accessed on 21 June 2021).

59. Babin, M.; Morel, A.; Fournier-Sicre, V.; Fell, F.; Stramski, D. Light scattering properties of marine particles in coastal and open ocean waters as related to the particle mass concentration. *Limnol. Oceanogr.* **2003**, *48*, 843–859. [CrossRef]

60. IOCCG. *Minimum Requirements for an Operational Ocean-Colour Sensor for the Open Ocean*; Morel, A., Ed.; Reports of the International Ocean-Colour Coordinating Group, No. 13; IOCCG: Dartmouth, NS, Canada, 1998.

61. IOCCG. *Mission Requirements for Future Ocean-Colour Sensors*; McClain, C.R., Meister, G., Eds.; Reports of the International Ocean-Colour Coordinating Group, No. 13; IOCCG: Dartmouth, NS, Canada, 2012; Available online: http://www.ioccg.org/reports/IOCCG_Report13.pdf (accessed on 23 June 2021).

62. Singh, R.K.; Shanmugam, P.; He, X.; Schroeder, T. UV-NIR approach with non-zero water-leaving radiance approximation for atmospheric correction of satellite imagery in inland and coastal zones. *Opt. Express* **2019**, *27*, A1118–A1145. [CrossRef]

63. Mobley, C.D.; Werdell, J.; Franz, B.; Ahmad, Z.; Bailey, S. Atmospheric correction for satellite ocean color radiometry. In *A Tutorial and Documentation NASA Ocean Biology Processing Group (Issue June)*; Goddart Space Flight Center: Greenbelt, MD, USA, 2016.

64. Mabit, R.; Araújo, C.A.S.; Singh, R.K.; Bélanger, S. Empirical Remote Sensing Algorithms to Retrieve SPM and CDOM in Québec Coastal Waters. *Front. Remote Sens.* **2022**, *3*, 834908. [CrossRef]

65. IOCCG. *Remote Sensing of Ocean Colour in Coastal, and Other Optically-Complex, Waters*; IOCCG: Dartmouth, NS, Canada, 2000.

66. Virtanen, P.; Gommers, R.; Oliphant, T.E.; Haberland, M.; Reddy, T.; Cournapeau, D.; Burovski, E.; Peterson, P.; Weckesser, W.; Bright, J.; et al. SciPy 1.0: Fundamental algorithms for scientific computing in Python. *Nat. Methods* **2020**, *17*, 261–272. [CrossRef]

67. Seegers, B.N.; Stumpf, R.P.; Schaeffer, B.A.; Loftin, K.A.; Werdell, P.J. Performance metrics for the assessment of satellite data products: An ocean color case study. *Opt. Express* **2018**, *26*, 7404–7422. [CrossRef]

68. Nordli, Ø. The Svalbard Airport Temperature Series. *Bull. Geography. Phys. Geogr. Ser.* **2010**, *3*, 5–25. [CrossRef]

69. Meteorologisk Institutt. Norsk Klimaservicesenter. Seklima. Observasjoner og værstatistikk. Available online: https://seklima.met.no/observations/ (accessed on 20 January 2022).

70. Kartverket—Norwegian Mapping Authority. Tidal and Water Level Data. Available online: https://www.kartverket.no/en/at-sea/se-havniva (accessed on 20 January 2022).

71. R Core Team. *R: A Language and Environment for Statistical Computing*; R Core Team: Vienna, Austria, 2021.

72. Hijmans, R.J. Raster: Geographic Data Analysis and Modeling. R package version 3.5-11. 2021. Available online: http://CRAN.R-project.org/package=raster (accessed on 15 June 2022).

73. Pierce, D. ncdf4: Interface to Unidata netCDF (Version 4 or Earlier) Format Data Files: R Package Version 1.18. 2021. Available online: https://CRAN.R-project.org/package=ncdf4 (accessed on 15 June 2022).

74. Ody, A.; Doxaran, D.; Vanhellemont, Q.; Nechad, B.; Novoa, S.; Many, G.; Bourrin, F.; Verney, R.; Pairaud, I.; Gentili, B. Potential of High Spatial and Temporal Ocean Color Satellite Data to Study the Dynamics of Suspended Particles in a Micro-Tidal River Plume. *Remote Sens.* **2016**, *8*, 245. [CrossRef]

75. Wei, T.; Simko, V. R package 'corrplot': Visualization of a Correlation Matrix. R paclage version 0.92. 2021. Available online: https://github.com/taiyun/corrplot (accessed on 23 June 2022).

76. Wickham, H. Reshaping Data with the reshape Package. *J. Stat. Softw.* **2007**, *21*, 1–20. [CrossRef]

77. Aphalo, P.J. ggpmisc: Miscellaneous Extensions to 'ggplot2'. 2021. Available online: https://CRAN.R-project.org/package=ggpmisc (accessed on 15 June 2022).

78. Wickham, H. *ggplot2: Elegant Graphics for Data Analysis*; Springer: New York, NY, USA, 2016; ISBN 978-3-319-24277-4.

79. Neuwirth, E. RColorBrewer: ColorBrewer Palettes. R package version 1.1-2. 2014. Available online: https://CRAN.R-project. org/package=RColorBrewer (accessed on 15 June 2022).

80. Bailey, S.W.; Werdell, P.J. A multi-sensor approach for the on-orbit validation of ocean color satellite data products. *Remote Sens. Environ.* **2006**, *102*, 12–23. [CrossRef]

81. Zajączkowski, M.; Włodarska-Kowalczuk, M. Dynamic sedimentary environments of an Arctic glacier-fed river estuary (Advent-fjorden, Svalbard). I. Flux, deposition, and sediment dynamics. *Estuar. Coast. Shelf Sci.* **2007**, *74*, 285–296. [CrossRef]

82. Rothenburg, M.A.J. The Advent River system, Central Svalbard: A High Temporal Resolution Analysis of Sediment Flux from a Dynamic Arctic River-Mouth. Master's Thesis, Vrije Universiteit, Amsterdam, The Netherlands, 2019.

83. Yde, J.C.; Riger-Kusk, M.; Christiansen, H.H.; Tvis Knudsen, N.; Humlum, O. Hydrochemical characteristics of bulk meltwater from an entire ablation season, Longyearbreen, Svalbard. *J. Glaciol.* **2008**, *54*, 259–272. [CrossRef]

84. Urbanski, J.A.; Stempniewicz, L.; Węsławski, J.M.; Dragańska-Deja, K.; Wochna, A.; Goc, M.; Iliszko, L. Subglacial discharges create fluctuating foraging hotspots for sea birds in tidewater glacier bays. *Sci. Rep.* **2017**, *7*, 1–12. [CrossRef] [PubMed]

85. Holding, J.M.; Markager, S.; Juul-Pedersen, T.; Paulsen, M.L.; Møller, E.F.; Meire, L.; Sejr, M.K. Seasonal and spatial patterns of primary production in a high-latitude fjord affected by Greenland Ice Sheet run-off. *Biogeosciences* **2019**, *16*, 3777–3792. [CrossRef]

86. Nowak, A.; Hodson, A. Hydrological response of a High-Arctic catchment to changing climate over the past 35 years: A case study of Bayelva watershed, Svalbard. *Polar Res.* **2013**, *32*, 19691. [CrossRef]

87. Huss, M.; Hock, R. Global-scale hydrological response to future glacier mass loss. *Nature Clim. Chang.* **2018**, *8*, 135–140. [CrossRef]

88. Jørgensen, B.B.; Laufer, K.; Michaud, A.B.; Wehrmann, L.M. Biogeochemistry and microbiology of high Arctic marine sediment ecosystems—Case study of Svalbard fjords. *Limnol. Oceanogr.* **2021**, *66*, S273–S292. [CrossRef]

89. Meire, L.; Mortensen, J.; Meire, P.; Juul-Pedersen, T.; Sejr, M.K.; Rysgaard, S.; Nygaard, R.; Huybrechts, P.; Meysman, F.J.R. Marine-terminating glaciers sustain high productivity in Greenland fjords. *Glob. Chang. Biol.* **2017**, *23*, 5344–5357. [CrossRef]

90. Hopwood, M.J.; Carroll, D.; Dunse, T.; Hodson, A.; Holding, J.M.; Iriarte, J.L.; Ribeiro, S.; Achterberg, E.P.; Cantoni, C.; Carlson, D.F.; et al. Review article: How does glacier discharge affect marine biogeochemistry and primary production in the Arctic? *Cryosphere* **2020**, *14*, 1347–1383. [CrossRef]

91. Bhatia, M.P.; Waterman, S.; Burgess, D.O.; Williams, P.L.; Bundy, R.M.; Mellett, T.; Roberts, M.; Bertrand, E.M. Glaciers and Nutrients in the Canadian Arctic Archipelago Marine System. *Global Biogeochem. Cycles* **2021**, *35*. [CrossRef]

92. Halbach, L.; Vihtakari, M.; Duarte, P.; Everett, A.; Granskog, M.A.; Hop, H.; Kauko, H.M.; Kristiansen, S.; Myhre, P.I.; Pavlov, A.K.; et al. Tidewater Glaciers and Bedrock Characteristics Control the Phytoplankton Growth Environment in a Fjord in the Arctic. *Front. Mar. Sci.* **2019**, *6*, 254. [CrossRef]

93. Mélin, F.; Vantrepotte, V. How optically diverse is the coastal ocean? *Remote Sens. Environ.* **2015**, *160*, 235–251. [CrossRef]

94. Yu, X.; Lee, Z.; Shen, F.; Wang, M.; Wei, J.; Jiang, L.; Shang, Z. An empirical algorithm to seamlessly retrieve the concentration of suspended particulate matter from water color across ocean to turbid river mouths. *Remote Sens. Environ.* **2019**, *235*, 111491. [CrossRef]

95. Blondeau-Patissier, D.; Gower, J.F.; Dekker, A.G.; Phinn, S.R.; Brando, V.E. A review of ocean color remote sensing methods and statistical techniques for the detection, mapping and analysis of phytoplankton blooms in coastal and open oceans. *Prog. Oceanogr.* **2014**, *123*, 123–144. [CrossRef]

96. Neukermans, G.; Loisel, H.; Mériaux, X.; Astoreca, R.; McKee, D. In situ variability of mass-specific beam attenuation and backscattering of marine particles with respect to particle size, density, and composition. *Limnol. Oceanogr.* **2012**, *57*, 124–144. [CrossRef]

97. Christiansen, H.H.; French, H.M.; Humlum, O. Permafrost in the Gruve-7 mine, Adventdalen, Svalbard. *Nor. Geogr. Tidsskr.-Nor. J. Geogr.* **2005**, *59*, 109–115. [CrossRef]

98. Ligi, M.; Kutser, T.; Kallio, K.; Attila, J.; Koponen, S.; Paavel, B.; Soomets, T.; Reinart, A. Testing the performance of empirical remote sensing algorithms in the Baltic Sea waters with modelled and in situ reflectance data. *Oceanologia* **2017**, *59*, 57–68. [CrossRef]

99. Jawak, S.D.; Andersen, B.N.; Pohjola, V.A.; Godøy, Ø.; Hübner, C.; Jennings, I.; Ignatiuk, D.; Holmén, K.; Sivertsen, A.; Hann, R.; et al. SIOS's Earth Observation (EO), Remote Sensing (RS), and Operational Activities in Response to COVID-19. *Remote Sens.* **2021**, *13*, 712. [CrossRef]